Electronic Supplementary Material (ESI) for Chemical Science

Supramolecular Mechanics in a Metal–Organic Framework

SUPPLEMENTARY INFORMATION

Joseph M. Ogborn,[1] Ines E. Collings,[1] Stephen A. Moggach,[2]
Amber L. Thompson[1] and Andrew L. Goodwin[1,*]

[1]Department of Chemistry, University of Oxford, Inorganic Chemistry Laboratory,
South Parks Road, Oxford OX1 3QR, U.K.
[2]Department of Chemistry, University of Edinburgh, Joseph Black Building,
The King's Buildings, West Mains Road, Edinburgh EH9 3JJ, U.K.
*Author to whom correspondence should be addressed;
E-mail andrew.goodwin@chem.ox.ac.uk

Contents

1 Single crystal structure determination.

Unit cell parameters, atom coordinates and isotropic displacement parameters for Ag(*mim*) as determined by single crystal X-ray diffraction are given in Tables S1 and S2 (100 K and 300 K, respectively)

Table S1. Crystallographic parameters, atomic coordinates and isotropic equivalent displacement parameters determined using single crystal X-ray diffraction data for Ag(*mim*) at 100 K.

Crystal system	Monoclinic			
Space group	$P2_1/n$			
a (Å)	7.6885(6)			
b (Å)	5.9097(4)			
c (Å)	10.9351(9)			
β (°)	92.984(3)			
V (Å^3)	496.18(7)			
Z	4			
T (K)	100			
Atom	x	y	z	U_{iso}*/U_{eq} (Å^2)
Ag1	0.5	0.5	0.5	0.0126
Ag2	0.5	1	1	0.0134
C1	0.3769(7)	0.9516(11)	0.6857(5)	0.0168
C2	0.4804(7)	0.7623(11)	0.7446(5)	0.0125
C3	0.6180(7)	0.4447(10)	0.7715(5)	0.0129
C4	0.6159(7)	0.5552(11)	0.8812(5)	0.0161
N1	0.5304(6)	0.5788(8)	0.6840(4)	0.0132
N2	0.5272(6)	0.7563(9)	0.8649(4)	0.0142
H13	0.3818	1.0811	0.7385	0.0251*
H12	0.4239	0.9917	0.6104	0.0245*
H11	0.2579	0.9062	0.6709	0.025*
H31	0.669	0.3048	0.7566	0.016*
H41	0.665	0.5026	0.9544	0.0189*

Table S2. Crystallographic parameters, atomic coordinates and isotropic equivalent displacement parameters determined using single crystal X-ray diffraction data for Ag(*mim*) at 300 K.

Crystal system	Monoclinic
Space group	$P2_1/n$
a (Å)	7.8946(6)
b (Å)	5.9692(4)
c (Å)	10.8812(10)
β (°)	92.454(3)
V (Å^3)	512.30(7)
Z	4
T (K)	300

Atom	x	y	z	U_{iso}*/U_{eq} (Å^2)
Ag1	0.5	0.5	0.5	0.0364
Ag2	0.5	1	1	0.0391
C1	0.3806(11)	0.9500(15)	0.6846(8)	0.0468
C2	0.4797(8)	0.7634(12)	0.7444(6)	0.0237
C3	0.6194(9)	0.4535(13)	0.7728(6)	0.032
C4	0.6155(10)	0.5588(13)	0.8805(6)	0.0371
N1	0.5320(7)	0.5817(10)	0.6841(4)	0.0281
N2	0.5286(8)	0.7588(10)	0.8653(5)	0.0296
H13	0.3919	1.0817	0.7334	0.0699*
H12	0.4197	0.9807	0.6051	0.0699*
H11	0.2647	0.909	0.6778	0.0701*
H31	0.6722	0.3164	0.7587	0.0381*
H41	0.6645	0.5086	0.954	0.0439*

2 Deformation mechanisms of Ag–*mim*–Ag linkages.

In order to assess the origin of negative thermal expansion along the c-axis, the thermal parameters and local geometry around Ag–*mim*–Ag were calculated. The anisotropic thermal parameters were constrained to be the same within the ligand for this particular analysis (though not for the full structure solutions), and the evolution of this displacement parameter as a function of temperature is shown in Figure S1. The vibrational motion of *mim* has two largest thermal components (U_{max} and U_{med}) which are along the directions perpendicular to the ligand, and midway between the latter and the plane of the ligand, see Figure S2. The smallest thermal component (U_{min}) is approximately along the Ag–*mim*–Ag bonding plane. These thermal components support the ligand displacement as transverse vibrations, which will contribute to the overall NTE observed along the c-axis. We note that the $\mathrm{d}U/\mathrm{d}T$ values obtained are close to those reported for the NTE material $Zn(CN)_2$, where they were used to substantiate the existence of a transverse-dispalcement-driven mechanism for NTE [*Phys. Rev. B* **71**, 140301 (2005)].

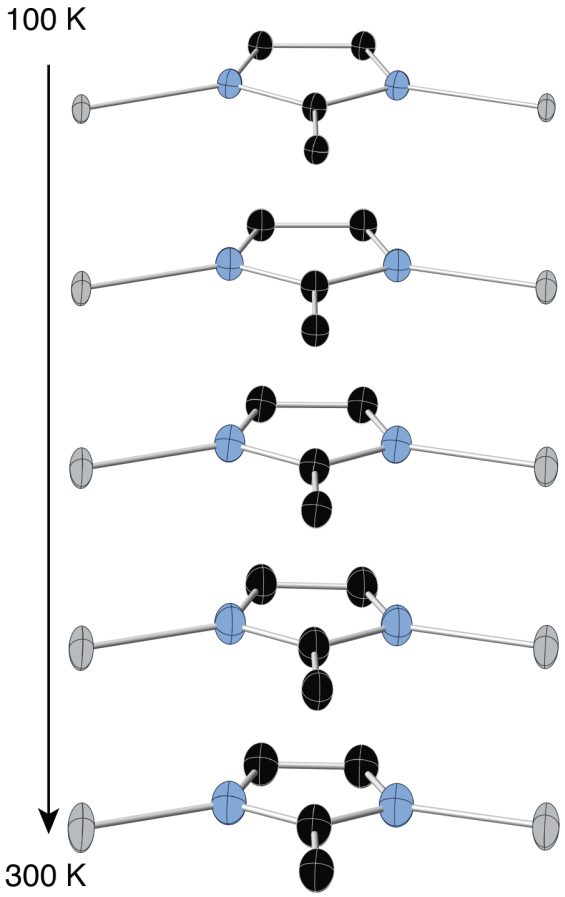

Figure S1. Ag–*mim*–Ag coordination environment shown with thermal ellipsoids at the 50% probability level as a function of temperature.

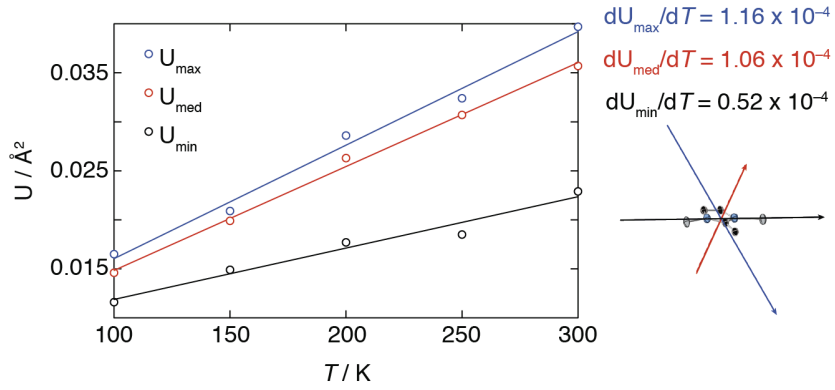

Figure S2. Principal components of the diagonalised anisotropic thermal parameters of 2-methylimidazolate as a function of temperature. The corresponding gradients and thermal parameter directions with respect to the ligand centroid are shown on the right of the graph.

The transverse vibration of the ligand has the effect of reducing the Ag–X distances (X=centroid of the imidazolate). In addition, the Ag–X distances become more symmetric, with the *mim* group adopting a more central position between the two silver atoms, see Figure S3. The coefficients of expansion for each geometric term as a function of temperature are listed in Table S3, and these numbers highlight the Ag–X changes which are associated with transverse vibrations as the largest NTE contributor.

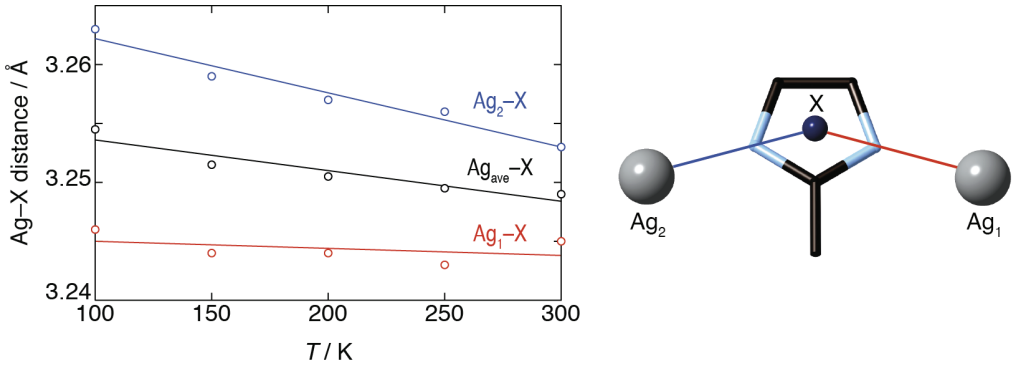

Figure S3. The evolution of Ag–X distances as a function of temperature, where X is the centroid of the imidazolate ring. The Ag_1-X, Ag_2–X and average of the two are shown.

As a function of pressure, the Ag−X distances are also found to decrease (see Figure S4), however, the Ag−*mim*−Ag angle now decreases considerably and is the main contributor for PLC (see Table S3). Consequently the mechanisms for Ag–*mim*–Ag compression under increasing temperature and pressure are not one and the same.

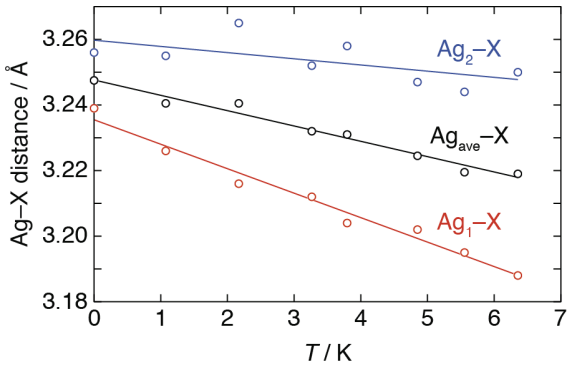

Figure S4. The evolution of Ag–X distances as a function of pressure, where X is the centroid of the imidazolate ring. The Ag_1-X, Ag_2–X and average of the two are shown.

Table S3. Geometric parameters analysed as a function of temperature and pressure, with coefficients of thermal expansion and compressibilities calculated via linear fits.

units	Ag–X–Ag angle	Ag_1–X	Ag_2–X	Ag_{ave}–X	Ag_1–Ag_2
MK^{-1}	0(4)	−14(2)	−2(2)	−8(2)	−8.4(4)
TPa^{-1}	5.8(5)	2.30(14)	0.6(3)	1.44(10)	3.89(8)

3 Variable-temperature lattice parameter data.

Variable-temperature lattice parameter data are given in Tables S4–S6, as determined using single crystal and powder X-ray diffraction.

Table S4. Variable-temperature lattice parameter data as determined using single crystal X-ray diffraction upon warming from 120 K to 300 K.

T (K)	*a* (Å)	*b* (Å)	*c* (Å)	β (°)	*V* (Å^3)
120	7.71(4)	5.911(24)	10.92(6)	92.9(4)	497(4)
140	7.7249(19)	5.9146(19)	10.907(3)	92.837(17)	497.71(25)
160	7.7500(19)	5.9277(18)	10.919(3)	92.842(16)	501.00(25)
180	7.7714(20)	5.9385(18)	10.921(3)	92.749(3)	503.42(25)
200	7.7843(21)	5.9294(18)	10.903(3)	92.684(16)	502.68(25)
220	7.8133(21)	5.9507(18)	10.907(3)	92.621(17)	506.59(25
240	7.8370(19)	5.9619(19)	10.897(3)	92.578(16)	508.64(25)
260	7.8477(20)	5.9455(20)	10.885(3)	92.574(16)	507.34(27)
280	7.8699(20)	5.9607(19)	10.883(4)	92.534(16)	510.03(29)
300	7.8969(20)	5.9784(19)	10.891(4)	92.506(17)	513.67(29)

Table S5. Variable-temperature lattice parameter data as determined using single crystal X-ray diffraction upon cooling from 300 K to 100 K.

T (K)	*a* (Å)	*b* (Å)	*c* (Å)	β (°)	*V* (Å^3)
300	7.8921(19)	5.9676(17)	10.884(3)	92.457(14)	512.14(24)
290	7.9001(20)	5.9936(20)	10.892(4)	92.486(16)	515.3(3)
280	7.8721(21)	5.9614(20)	10.887(4)	92.522(16)	510.4(3)
270	7.8599(20)	5.9511(19)	10.878(4)	92.563(15)	508.27(28)
260	7.8469(20)	5.9450(19)	10.882(3)	92.569(15)	507.12(26)
250	7.8401(6)	5.9549(4)	10.8935(10)	92.5560(3)	508.08(7)
240	7.8328(18)	5.9582(17)	10.8985(28)	92.595(13)	508.10(23)
230	7.8221(19)	5.9546(17)	10.901(3)	92.594(14)	507.23(24)
220	7.812(18)	5.9529(15)	10.9005(28)	92.618(12)	506.39(22)
210	7.8016(17)	5.9458(15)	10.9057(26)	92.633(13)	505.35(21)
200	7.7899(6)	5.9402(4)	10.9075(10)	92.670(3)	504.18(7)
190	7.7752(16)	5.9239(17)	10.906(3)	92.728(14)	501.77(23)
180	7.7672(17)	5.9305(17)	10.9123(29)	92.726(13)	502.09(22)
170	7.7569(18)	5.9293(17)	10.916(3)	92.749(13)	501.46(23)
160	7.7488(18)	5.9310(17)	10.919(3)	92.823(13)	501.20(23)
150	7.7365(19)	5.9237(18)	10.917(3)	92.890(14)	499.67(25)
140	7.7275(18)	5.9197(18)	10.914(3)	92.863(14)	498.64(24)
130	7.7162(19)	5.9096(18)	10.919(3)	92.883(16)	497.25(24)
120	7.7070(17)	5.9087(16)	10.9265(29)	92.941(14)	496.92(22)
110	7.6962(17)	5.9061(16)	10.926(3)	92.939(15)	495.97(22)
100	7.6907(18)	5.9094(16)	10.9315(27)	92.963(15)	496.14(22)

Table S6. Variable-temperature lattice parameter data as determined using powder X-ray diffraction upon cooling from 150 K to 20 K.

T (K)	*a* (Å)	*b* (Å)	*c* (Å)	β (°)	*V* (Å^3)
150	7.7396(8)	5.9360(11)	10.9243(21)	92.715(20)	501.32(14)
140	7.7253(10)	5.9308(13)	10.9237(26)	92.745(26)	499.92(17)
130	7.7168(8)	5.9300(10)	10.9296(20)	92.787(20)	499.55(13)
120	7.7066(7)	5.9247(10)	10.9313(20)	92.834(18)	498.50(13)
110	7.6978(7)	5.922(10)	10.9343(20)	92.881(18)	497.83(13)
100	7.6874(7)	5.9186(10)	10.9358(19)	92.946(18)	496.91(13)
90	7.679(7)	5.9161(10)	10.9365(19)	92.980(18)	496.17(13)
80	7.6718(7)	5.9148(10)	10.9379(19)	93.007(18)	495.65(13)
70	7.6645(7)	5.9105(10)	10.9408(19)	93.023(19)	494.94(13)
60	7.6581(7)	5.9095(10)	10.9428(19)	93.023(19)	494.53(13)
50	7.6533(7)	5.9063(10)	10.9443(19)	93.053(19)	494.01(13)
40	7.6499(7)	5.9057(10)	10.9458(19)	93.060(18)	493.80(13)
30	7.6473(7)	5.9046(9)	10.9471(19)	93.058(18)	493.60(12)
20	7.6444(7)	5.9020(10)	10.9477(20)	93.070(19)	493.22(13)

4 Variable-pressure lattice parameter data.

Variable-pressure lattice parameter data are given in Table S7, as determined using single crystal X-ray diffraction.

Table S7. Variable-pressure lattice parameter data as determined using single crystal X-ray diffraction.

p (GPa)	*a* (Å)	*b* (Å)	*c* (Å)	β (°)	*V* (Å)
0	7.8926(5)	5.9767(3)	10.8739(6)	92.470(5)	512.46(5)
0.305(5)	7.726(5)	5.9233(10)	10.888(2)	92.73(3)	497.7(4)
1.08(8)	7.433(2)	5.8092(3)	10.9101(5)	93.736(10)	470.09(13)
2.17(14)	7.2027(16)	5.6926(3)	10.9057(4)	94.504(8)	445.78(10)
3.27(8)	7.0544(17)	5.6024(3)	10.8873(4)	95.062(9)	428.61(11)
3.80(16)	6.9920(13)	5.5590(2)	10.8750(4)	95.344(7)	420.86(8)
4.85(4)	6.9259(16)	5.5072(2)	10.8549(4)	95.667(8)	412.01(10)
5.6(3)	6.8710(13)	5.4670(2)	10.8393(3)	95.878(7)	405.02(8)
6.4(4)	6.828(2)	5.4298(3)	10.8209(5)	96.076(11)	398.92(12)

5 Empirical fitting of lattice expansivity and compressibility values.

Inspection of the experimental variable-temperature lattice parameter data reveals significant nonlinearity at low temperatures. Consequently linear fits do not capture well this low-temperature behaviour, which can lead to the extraction of expansivity values that do not reflect fully the real mechanical property of the material in question. Consequently, we have used an empirical expression of the form

$$x(T) = x_0 + \kappa T \left(\frac{T}{T - T_c} \right)^{\lambda}, \tag{1}$$

which has been chosen so as to fit the observed curvature at low temperature with a minimum of parameters $(x_0, \kappa, T_c, \lambda)$. Moreover, the derivative obeys the the thermodynamic requirement

$$\left. \frac{dx}{dT} \right|_{T=0\,K} = 0. \tag{2}$$

For similar reasons, we have fitted the compressibility data using an empirical expression of the form

$$x(p) = x_0 + \kappa |p - p_c|^{\lambda}. \tag{3}$$

The numerical expansivities and compressibilities values, shown in Table 1 (main text), were obtained via linear fits using PASCal, using orthogonal lattice parameter evolution, see Figure S5-S7. In these graphs $\mathbf{x}_1 = \sim \mathbf{a}$, $\mathbf{x}_2 = \mathbf{b}$ and $\mathbf{x}_3 = \sim \mathbf{c}$.

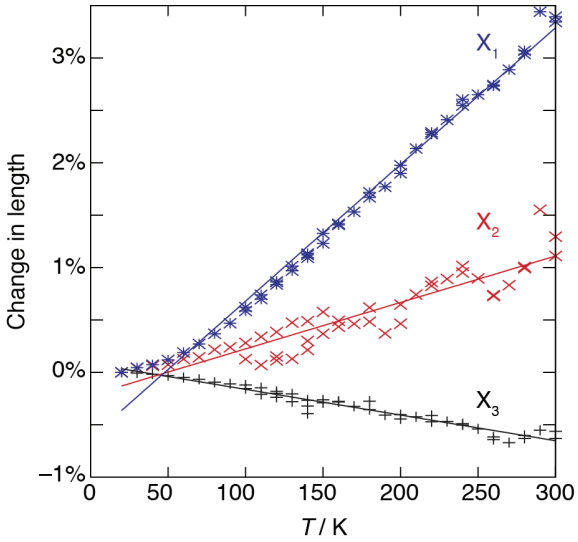

Figure S5. Linear fits to lattice parameter evolution as a function of temperature obtained using PASCal.

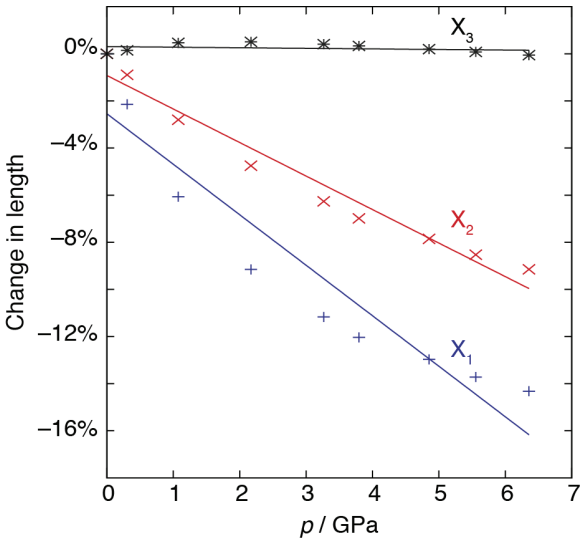

Figure S6. Linear fits to the lattice parameter evolution as a function of pressure obtained using PASCal using the full pressure range.

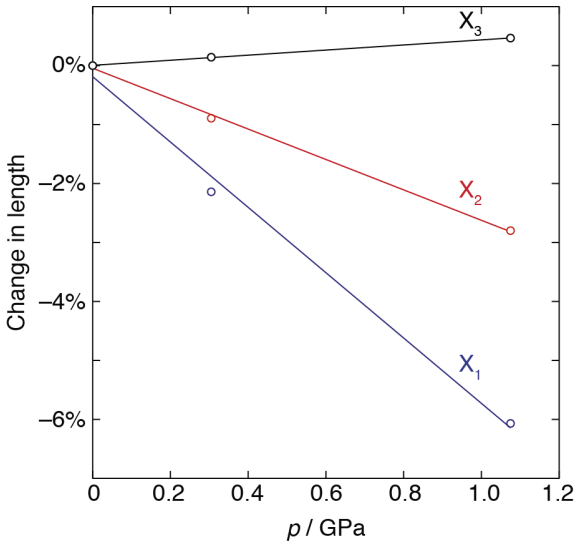

Figure S7. Least-squares linear fits to the pressure-dependent principal strains (0−1 GPa) obtained by orthogonalisation of the compressibility tensor using PASCal.

6 Principal-axis analysis of expansivity and compressibility tensors.

The principal-axis expansivities and compressibilities, obtained via empirical fitting of the raw lattice parameter data, are given in Tables S8 and S9, respectively.

Table S8. Expansivities obtained via empirical fits.

T (K)	α_1 (MK^{-1})	α_2 (MK^{-1})	α_3 (MK^{-1})
30	27.9	9.2	−8.1
40	48.1	15.9	−11.6
50	65.6	21.7	−14.3
60	79.8	26.4	−16.2
70	91.1	30.2	−17.7
80	100.1	33.1	−18.7
90	107.2	35.5	−19.6
100	112.9	37.5	−20.2
100	113.0	37.5	−20.2
110	117.7	39.2	−20.8
110	117.6	39.0	−20.8
120	121.5	40.5	−21.2
120	121.4	40.4	−21.2
120	121.5	40.3	−21.2
130	124.6	41.6	−21.5
130	124.6	41.4	−21.5
140	127.2	42.4	−21.8
140	127.3	42.4	−21.9
140	127.3	42.3	−21.8
150	129.4	43.2	−22.1
150	129.4	43.1	−22.0
160	131.2	43.8	−22.3
160	131.2	43.8	−22.3

T (K)	α_1 (MK^{-1})	α_2 (MK^{-1})	α_3 (MK^{-1})
170	132.8	44.4	−22.4
180	134.2	44.9	−22.6
180	134.1	44.8	−22.6
190	135.4	45.4	−22.7
200	136.3	45.6	−22.8
200	136.4	45.7	−22.9
210	137.1	45.9	−22.9
220	137.8	46.2	−23.0
220	137.8	46.2	−23.0
230	138.4	46.4	−23.1
240	138.9	46.6	−23.2
240	138.9	46.6	−23.2
250	139.4	46.9	−23.3
260	139.9	47.2	−23.3
260	139.9	47.2	−23.3
270	140.2	47.3	−23.4
280	140.4	47.4	−23.4
280	140.5	47.4	−23.4
290	140.4	47.3	−23.4
300	140.9	47.6	−23.5
300	140.8	47.5	−23.5

Table S9. Compressibilities obtained via empirical fits.

p (GPa)	K_a (TPa^{-1})	K_b (TPa^{-1})	K_c (TPa^{-1})
0.305	66.4	42.0	-2.2
1.075	35.4	21.1	-1.7
2.17	21.7	15.1	2.1
3.265	15.8	12.5	2.3
3.795	14.0	11.7	2.4
4.85	11.4	10.5	2.5
5.555	10.2	9.8	2.6
6.355	9.1	9.3	2.6

The assertion is made in the text that the principal axes are oriented closely to the unit cell axes as chosen. In full detail, we find that the principal and lattice axes are related by the matrix algebra

$$\begin{bmatrix} \mathbf{x}_1 \\ \mathbf{x}_2 \\ \mathbf{x}_3 \end{bmatrix} = \begin{bmatrix} 0.9892 & 0 & -0.1467 \\ 0 & 1 & 0 \\ -0.1085 & 0 & -0.9941 \end{bmatrix} \begin{bmatrix} \mathbf{a} \\ \mathbf{b} \\ \mathbf{c} \end{bmatrix}$$

in the case of the variable-temperature data, and by

$$\begin{bmatrix} \mathbf{x}_1 \\ \mathbf{x}_2 \\ \mathbf{x}_3 \end{bmatrix} = \begin{bmatrix} 0.9875 & 0 & 0.1573 \\ 0 & -1 & 0 \\ 0.2414 & 0 & -0.9704 \end{bmatrix} \begin{bmatrix} \mathbf{a} \\ \mathbf{b} \\ \mathbf{c} \end{bmatrix}$$

in the case of the variable-pressure data. In both cases, the deviation of $\mathbf{x}_1$ and $\mathbf{x}_3$ away from the a and c-axes is less than 3%.

7 Negative to positive linear compressibility transition.

Two XBUs contribute to the compressibility observed along the c-axis: on the one hand, compression of the strut XBUs causes a contraction along $\mathbf{c}$ with increasing pressure; on the other hand the reduction in θ with increasing pressure translates to an *increase* in $\mathbf{c}$. Figure S6 shows the relative magnitudes of these two contributions as a function of pressure, obtained via the empirical fits as described in the main text. What we find is that magnitude of the negative compressibility effect attributable to K_θ dominates only for pressures below about 1.5 GPa; hence the material as a whole shows NLC along the c-axis for this pressure regime alone. For pressures $p > 1.5$ GPa, the positive compressibility attributable to K_r dominates and the material shows PLC behaviour along $\mathbf{c}$.

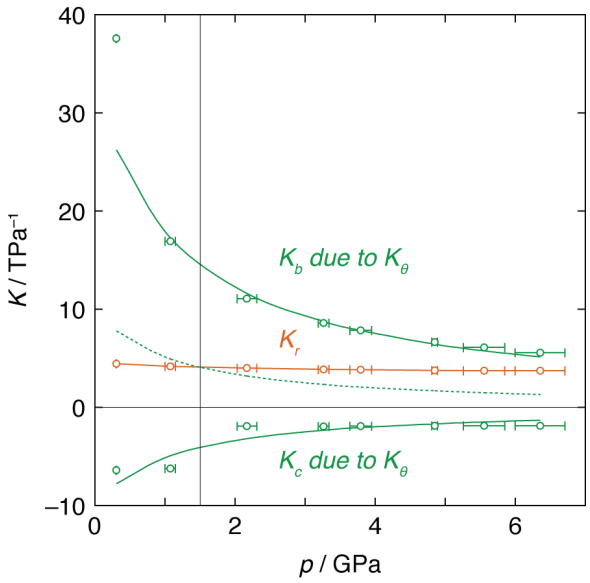

Figure S8. Compressibilities obtained via empirical fits: the XBU compressibility K_r associated with compression of the Ag–*mim*–Ag struts is shown in orange, and the axial compressibilities K_b and K_c attributable to the XBU compressibility K_θ are shown in green. The dashed green line is the negative of the "K_c due to K_θ" line; its point of intersection with the K_r curve represents the pressure value at which the lattice compressibility along $\mathbf{c}$ switches from negative to positive behaviour.

In determining the contributions of K_θ to K_b and K_c we have made use of the following relations:

$$b = 2r\sin\theta, \tag{4}$$

$$c = 2r\cos\theta, \tag{5}$$

$$K_b \text{ due to } K_\theta = -\frac{1}{b}\left(\frac{\partial b}{\partial p}\right)_r = -\frac{2r}{b}\cos\theta\frac{\partial\theta}{\partial p} = \frac{c}{b}\theta K_\theta, \tag{6}$$

$$K_c \text{ due to } K_\theta = -\frac{1}{c}\left(\frac{\partial c}{\partial p}\right)_r = \frac{2r}{c}\sin\theta\frac{\partial\theta}{\partial p} = -\frac{b}{c}\theta K_\theta. \tag{7}$$

8 $\Delta H_{1\%}$ calculations.

Force-constant data for ligand-unsupported argentophilic systems are surprisingly rare. Better studied are the aurophilic analogues, for which typical Au. . .Au force constants are 0.15 mdyn Å^{-1} for an internuclear separation of *ca* 3.0 Å [*J. Am. Chem. Soc.* **123**, 11237 (2001)]. For ligand-supported argentophilic interactions, the ratio of Ag. . .Ag:Au. . .Au force constants is 0.203:0.449, which suggests a ligand-unsupported argentophilic force constant of approximately 0.07 mdyn Å^{-1}. Taking a typical Ag. . .Ag separation of 3.2 Å, then a 1% strain corresponds to an energy change of 41 J mol^{-1}.

In order to estimate framework flexing energies, we made use of the dispersive-uncorrected DFT results of Calleja *et al.* for $Ag_3[Co(CN)_6]$ [*J. Phys.: Condens. Matt.* **20**, 255226 (2008)]. In that study, the system free energy was calculated for an array of lattice parameter values, with the lattice-flexing distortion tracing out a low-enthalpy "valley" in phase space. A quadratic fit to the free energy within this valley according to the expression

$$E(a) = E_0 + \alpha(a - a_0)^2 \tag{8}$$

gives parameters $E_0 = 247$ meV, $\alpha = 185$ meV Å^{-2} and a_0 =7.58 Å. Consequently, a 1% linear strain in the lattice parameter corresponds to a free energy change of 1.1 meV or 103 J mol^{-1}. Finally, the molecular modelling parameters used in a study of ZIF-8 (composition $Zn(im)_2$) [*Phys. Rev. Lett.* **104**, 115503 (2010)] were used to estimate the energy cost of a 1% strain in the Ag–*mim*–Ag linkage through transverse displacements as described in Section 2. The basic form of the angular potential is

$$E = \frac{1}{2}K\left(\cos\theta - \cos\theta_0\right)^2 \tag{9}$$

with Ag–N–C angle force constant K = 20 eV and ground-state Ag–N–C angle θ_0 = 120°. Straightforward trigonometry gives that a 1% reduction in the Ag. . .Ag separation by transverse displacement of the 2-methylimidazolate anion corresponds to a reduction in θ by 0.8°. The corresponding energy penalty (noting that two Ag–N–C angles are affected) is 270 J mol^{-1}.